Oblique collision of two vortex rings and its acoustic emission

T. Kambe
Department of Physics, University of Tokyo, Hongo, Bunkyo-ku, Tokyo 113, Japan

T. Minota
Ariake National College of Technology, Higasi-Hagio, Omuta, Fukuoka 836, Japan

M. Takaoka
Department of Mechanical Engineering, Osaka University, Toyonaka, Osaka 560, Japan
(Received 16 April 1993)

A theory of vortex sound is formulated in the form of multipole expansions and an explicit formula is presented for the wave pressure excited by a time-dependent vorticity field localized in space. This is applied to the case of the oblique collision of two vortex rings at right angles, in which higher-order terms are important to represent asymmetric emission. The vortex motion and the generated waves are also studied experimentally and numerically. The initial setup of the two vortices is arranged so that they come into contact by their own motions and perform a reconnection of the vortex lines. The acoustic waves generated by the vortex motion have been observed in the far field in the laboratory, and the detected pressure signals are represented as a series of several dominant modes of the spherical harmonics. Morphological development of the vortices and trajectories of the vortex cores in the collision process are observed by optical means. Computer simulation of the vortex motion has been carried out for a viscous incompressible fluid at a lower Reynolds number than that of the experiment. The evolution of the vorticity field thus obtained can be used to predict the wave profile by using the theoretically derived formula. The corresponding wave modes, obtained from both laboratory experiment and computer simulation independently, are compared. It is remarkable that two main quadrupole modes (two second-order spherical harmonics) are in qualitative agreement between the two cases. Third-order modes are also estimated, and one mode is responsible for the characteristic emission of asymmetric waves observed in the experiment, which is associated with the details of the collision process.

PACS number(s): 47.32.Cc, 43.28.+h, 47.10.+g

I. INTRODUCTION

Wave generation by a vortex motion is studied, based on the fundamental equations of motion at low Mach numbers and high Reynolds numbers. The physical idea is as follows. Suppose that there exists an unsteady fluid motion with a localized vorticity field $\boldsymbol{\omega}$ of a length scale l, inducing an approximately solenoidal field of velocity $\mathbf{v}$ of a typical magnitude u. Pressure fluctuations are excited at large distances by the vortex motion. These drive acoustic waves. The source flow is surrounded by an outer wave field scaled on the length $\lambda = c\tau$, where c is the sound speed in the undisturbed medium at rest and $\tau = l/u$ is a typical time scale of the vortex motion. Typical Mach number M is assumed to be much less than unity:

$$M = u/c \ll 1 \quad .$$

Owing to this condition, the whole field is separated into two fields: *inner* flow and *outer* wave regions because the wave scale $\lambda = l/M$ is much larger than the vortex scale l. Theory of vortex sound is developed under these circumstances [1–9,27].

Collision of two vortex rings is a typical example of three-dimensional vortex interactions which can be studied both experimentally and computationally. In the past experimental studies of observing the acoustic waves were carried out for the head-on collision of two vortex rings [7,10]. The setup of head-on collsion has an axisymmetric property, while the oblique collision of two vortex rings studied here has no such symmetry. This requires an increased amount of tasks in order to study the details of the motion and analyze the detected wave signals both experimentally and computationally (see Ref. [11], a preliminary report of the study). In such a collision at a high Reynolds number, we expect far more complex interaction, including the contact sand reconnection of antiparallel vortex lines. As is considered in the subsequent sections, this event is associated with an energetic motion of vortex lines, resulting in excitation of asymmetric waves. Hence the analysis of the wave data provides indirect (or remote sensing) information about the time evolution of the complex vortex motion.

The mechanical process of sound generation is formulated mathematically, and explicit formulas of the wave profile are given in terms of the time-dependent vorticity field. Study of the vortex sound using vortex rings has been made in the past decade for various experimental arrangements, and the results are reported in Ref. [8] for three typical problems of acoustic emission: (i) by head-on collision, (ii) by a vortex ring passing nearby a

circular cylinder, and (iii) by one passing nearby a sharp edge. Studies are also made for a sphere [12] and for a finite plate [13]. Note that an optical observation is made for the acoustic waves generated by a rectilinear vortex impinging on an aerofoil [14]. The vortex sound theory is also reviewed in Refs. [9,27].

The geometry of the vortex motion studied in this paper is as follows. Initial state is given in such a way that two vortex rings are set to move along the paths intersecting at right angles and collide with each other in due course. Two independent studies are presented here: one is an experimental observation of the acoustic waves generated by the two-vortex collision (Sec. III), and the other is a numerical simulation of the same problem based on the Navier-Stokes equation but at a lower Reynolds number. Although this numerical simulation is carried out for an *incompressible* fluid motion, this is useful in the present wave problem to obtain the wave profile in an asymptotic sense (Sec. IV), since the coefficients in the formula are also derived by using the solenoidal property of the inner velocity field. New general mathematical formulation is presented in Sec. II, in which a formula of the wave pressure generated by a vortex motion is given consistently in the form of multipole expansions to any order. With using this formula, the component waves are estimated numerically by the computed vortex motion. These are compared with the ones derived from the observation (Sec. V). The observed wave signals show existence of the third-order component (octupole), which is a new feature and is discussed in Sec. VI.

II. MATHEMATICAL FORMULATION

We present here a general formulation, in which a multipole expansion is carried out to any order n. Suppose that there exists an unsteady fluid motion having a localized time-dependent vorticity $\boldsymbol{\omega}(\mathbf{x},t)$ characterized with the scales l and u in the otherwise uniform fluid at rest of density ρ_0 and pressure p_0, where the term *localized* means that $\boldsymbol{\omega}$ decays exponentially as the distance $|\mathbf{x}|/l$ tends to infinity. Due to the unsteady vorticity field of the time scale $\tau = l/u$, pressure fluctuations will be generated at large distances, giving rise to acoustic waves.

A. Governing equations

The basic equation of the aerodynamic sound generation is given by Lighthill [15] in the form of the inhomogeneous wave equation for the density ρ:

$$\frac{\partial^2\rho}{\partial t^2} - c^2\nabla^2\rho = \frac{\partial^2}{\partial x_i \partial x_j} T_{ij}, \tag{1}$$

where

$$T_{ij} = \rho v_i v_j + (p - c^2\rho)\delta_{ij} - \tau_{ij} \ ,$$

v_i is the ith component of the velocity $\mathbf{v}$, p the pressure, and τ_{ij} the viscous stress tensor. Summation convention is assumed on the right-hand side (RHS) for the repeated indices taking 1, 2, and 3.

In the inner region scaled by the length l and the time τ, the ratio of the two terms on the left-hand side (LHS) is estimated as

$$\frac{|\rho_{tt}|}{|c^2\nabla^2\rho|} = O\left(\frac{\tau^{-2}}{c^2 l^{-2}}\right) = O(M^2) \ .$$

In the first approximation neglecting the terms of $O(M^2)$ and hence the term ρ_{tt}, we have

$$-\nabla^2 p = \rho_0 \partial_i \partial_j \ (v_i v_j) \ , \tag{2}$$

where $\partial_i = \partial/\partial x_i$. This is equivalent to the Navier-Stokes equation for an incompressible fluid:

$$\rho_0 \, \partial_t v_i + \rho_0 \, v_j \partial_j \, v_i = -\partial_i \, p + \partial_j \, \tau_{ji} \ , \tag{3}$$

$$\operatorname{div} \mathbf{v} = 0 \ , \tag{4}$$

where $\partial_t = \partial/\partial t$. In fact, taking the divergence of (3) under the solenoidal condition (4) yields the equation (2), where we have used $\partial_i \partial_j \, \tau_{ji} = 0$ since $\tau_{ji} = \mu(\partial_i v_j + \partial_j v_i)$ for an incompressible fluid with a constant shear viscosity μ.

In the outer region where the fluid velocity $|\mathbf{v}|$ decays rapidly, the equation of motion can be linearized with respect to the perturbation velocity, and the adiabatic relation, $p - p_0 = c^2(\rho - \rho_0)$, is satisfied approximately, since the viscosity effect is much smaller and estimated as

$$\frac{|\partial_j \, \tau_{ji}|}{|\rho_0 \, \partial_t v_i|} = O\left(\frac{\mu\lambda^{-2}}{\rho_0 \tau^{-1}}\right) = O(Re^{-1}M^2) \ ,$$

where $Re = ul/\nu$ ($\gg 1$, assumed) is the Reynolds number of the inner source flow, and $\nu = \mu/\rho_0$. Thus the RHS of the equation (1) is neglected in the leading order of approximation, and the pressure p is governed by the wave equation:

$$\frac{1}{c^2}\frac{\partial^2 p}{\partial t^2} - \nabla^2 p = 0 \tag{5}$$

(Ref. [8]). The wave region is characterized by an outer variable, defined by $\hat{\mathbf{x}} \equiv \mathbf{x}/\lambda$, taking values of order unity in the outer region.

An inner problem is solved first to represent the source flow of a viscous vortex motion. Then an outer solution is sought so as to match the inner solution just obtained. This solution represents an acoustic wave emitted by the vortex motion, which is called the vortex sound.

B. Asymptotic formula of the vortex sound

Suppose that the vorticity field $\boldsymbol{\omega}(\mathbf{x},t) = \boldsymbol{\nabla} \times \mathbf{v}$ satisfies the equation,

$$\partial_t \boldsymbol{\omega} - \nabla \times (\mathbf{v} \times \boldsymbol{\omega}) = \nu \nabla^2 \boldsymbol{\omega} \ , \tag{6}$$

derived from the Navier-Stokes equations (3) and (4). It is convenient to introduce a vector potential $\mathbf{A}(\mathbf{x},t)$ and a scalar potential $\Phi_0(\mathbf{x},t)$ for the velocity $\mathbf{v}(\mathbf{x},t)$ by the (Helmholtz) decomposition, $\mathbf{v} = \nabla \times \mathbf{A} + \nabla \Phi_0$, where the first term represents the solenoidal part associated with the vorticity $\boldsymbol{\omega}(\mathbf{x},t)$ and the second term represents fluid compressibility or presence of a solid body in the inner region. From this we have $\boldsymbol{\omega} = \nabla \times \mathbf{v} = \nabla \times (\nabla \times \mathbf{A}) = -\nabla^2 \mathbf{A}$, assuming the gauge condition $\nabla \cdot \mathbf{A} = 0$. Therefore the vector potential $\mathbf{A}$ is given by

$$\mathbf{A}(\mathbf{x},t) = \frac{1}{4\pi} \int \frac{\boldsymbol{\omega}(\mathbf{y},t)}{|\,\mathbf{x}-\mathbf{y}\,|} d^3\mathbf{y} \quad .$$

The vector $\mathbf{x} = (x_i)$ is used for the point of observation and $\mathbf{y} = (y_i)$ for the point of integration (or the source point). The factor $1/|\mathbf{x}-\mathbf{y}|$ can be expanded in a Taylor series with respect to y_i/r for sufficiently large $r = |\mathbf{x}|$, which is convergent for $|\mathbf{y}|/|\mathbf{x}| < 1$. Thus we obtain

$$A_k(\mathbf{x},t) = \frac{1}{4\pi} \sum_{n=1}^{\infty} \frac{(-1)^n}{n!} \sum_{p_1} \cdots \sum_{p_n} W^k_{p_1 \cdots p_n} \partial_{p_1} \cdots \partial_{p_n} \frac{1}{r} \ , \tag{7}$$

where

$$W^k_{p_1 \cdots p_n}(t) = \int \omega_k(\mathbf{y},t)\ y_{p_1} \cdots y_{p_n} d^3\mathbf{y} \quad . \tag{8}$$

The solenoidal part of the velocity is expressed by $v_i^{(s)} = \epsilon_{ijk}\, \partial_j A_k$, where ϵ_{ijk} is the third-order skew symmetric tensor. The velocity field $\mathbf{v}^{(s)}(\mathbf{x},t)$ approaches asymptotically to such a field as represented by a velocity potential $\Phi^{(s)}$ as $|\mathbf{x}| \to \infty$.

After some substantial calculation (see Appendix), an asymptotic expansion of the velocity is given in the form

$$v_i^{(s)}(\mathbf{x},t) = \partial_i \Phi^{(s)}, \quad \Phi^{(s)} = \sum_{n=1}^{\infty} \Phi_n, \tag{9}$$

where

$$\Phi_n = \sum_{p_1} \cdots \sum_{p_n} Q_{p_1 \cdots p_n}(t)\ \partial_{p_1} \cdots \partial_{p_n} \frac{1}{r} \ , \tag{10}$$

$$Q_{p_1 \cdots p_n}(t) = \frac{(-1)^{n+1} n}{4\pi (n+1)!} \int (\mathbf{y} \times \boldsymbol{\omega})_{p_1} y_{p_2} \cdots y_{p_n} d^3\mathbf{y} \tag{11}$$

$(n = 1, 2, \ldots)$. Thus we find that an asymptotic expression of the total velocity in the inner region is given in the form, $\mathbf{v}^{(i)} = \text{grad}\, \Phi$, where

$$\Phi(\mathbf{x},t) = \Phi_0(\mathbf{x},t) + Q_i\, \partial_i \frac{1}{r} + Q_{ij}\, \partial_i \partial_j \frac{1}{r} + Q_{ijk}\, \partial_i \partial_j \partial_k \frac{1}{r} + O(r^{-5}) \ , \tag{12}$$

and the first few terms (the first term Φ_0 being considered below) are

$$\Phi_1 = \sum_{i=1}^{3} Q_i(t) \frac{\partial}{\partial x_i} \frac{1}{r} \ , \quad Q_i(t) = \frac{1}{8\pi} \int (\mathbf{y} \times \boldsymbol{\omega})_i\, d^3\mathbf{y} \ , \tag{13}$$

$$\Phi_2 = \sum_i \sum_j Q_{ij}(t) \frac{\partial^2}{\partial x_i \partial x_j} \frac{1}{r} \ , \tag{14}$$

$$Q_{ij}(t) = -\frac{1}{12\pi} \int (\mathbf{y} \times \boldsymbol{\omega})_i\, y_j\, d^3\mathbf{y} \ ,$$

$$\Phi_3 = \sum_i \sum_j \sum_k Q_{ijk}(t) \frac{\partial^3}{\partial x_i \partial x_j \partial x_k} \frac{1}{r} \ , \tag{15}$$

$$Q_{ijk}(t) = \frac{1}{32\pi} \int (\mathbf{y} \times \boldsymbol{\omega})_i\, y_j\, y_k\, d^3\mathbf{y} \ ,$$

the two potentials Φ_1 and Φ_2 being already given explicitly in Ref. [16]. It is almost trivial to show the following properties:

$$Q_{ii}(t) = 0 \ , \quad Q_{iik}(t) = 0 \ , \quad Q_{iji}(t) = 0 \tag{16}$$

by the orthogonality of the two vectors $\mathbf{y}$ and $\mathbf{y} \times \boldsymbol{\omega}$. The resultant impulse of the vortex system is defined by $4\pi Q_i$, which is an invariant of motion for unbounded fluid without external body (see Sec. VI).

The compressibility of the inner source flow [$|\text{div}\, \mathbf{v}^{(i)}|$ being $O(M^2)$ and of scale l] is assumed to be localized and represented by Φ_0, while the generated acoustic wave is of larger scale $\lambda (\gg l)$ and treated in the next stage. From the theory of irrotational motion with a localized rate of expansion $\Theta(\mathbf{x},t) = \text{div}\, \mathbf{v}^{(i)}$, the first term Φ_0 is given by the following asymptotic expression [17]:

$$\Phi_0 = R_0(t) \frac{1}{r} + R_i(t)\, \partial_i \frac{1}{r} + R_{ij}(t)\, \partial_i \partial_j \frac{1}{r} + R_{ijk}(t)\, \partial_i \partial_j \partial_k \frac{1}{r} + O(r^{-5}) \ , \tag{17}$$

where $R_0, R_i, R_{ij}, \ldots$ are all functions of time t and determined by the distribution of $\Theta(\mathbf{x},t)$.

The presence of a solid body in the vicinity of the vortex motion can be represented by an additional velocity potential whose asymptotic expression is again of the form (17) (see, e.g., Ref. [17], Chap. 2.9). In the case of solid body, the first monopole term must vanish by the condition of no net outflow over the body surface. Thus both effects of compressibility and presence of solid body are represented by the expansion (17).

At large distances from the region of vortex motion, the equation of motion will be linearized with respect to the velocity, and the viscosity terms will be neglected because of the higher order of the space derivatives. Thus we have $\rho_0\, \partial_t \mathbf{v}^{(i)} = -\text{grad}\, p^{(i)}$, where $\mathbf{v}^{(i)} = \text{grad}\, \Phi$. Accordingly, the asymptotic form of the inner pressure $p^{(i)}$ is given by $p^{(i)} = -\rho_0\, \partial_t \Phi$, namely

$$p^{(i)}(\mathbf{x},t) = -\rho_0 \dot{P}_0 \frac{1}{r} - \rho_0 \dot{P}_i\, \partial_i \frac{1}{r} - \rho_0 \dot{P}_{ij}\, \partial_i \partial_j \frac{1}{r} - \rho_0 \dot{P}_{ijk}\, \partial_i \partial_j \partial_k \frac{1}{r} + O(r^{-5}) \ , \tag{18}$$

where a dot denotes a time differentiation, and

$$P_0(t) = R_0\,,\ P_i(t) = Q_i + R_i\,,\ P_{ij}(t) = Q_{ij} + R_{ij}\,,$$

$$P_{ijk}(t) = Q_{ijk} + R_{ijk}\,,\ \cdots\ .$$

A general solution to the wave equation (5) is represented in the form of multipole expansion [4,8], valid in the outer wave region for $|\hat{\mathbf{x}}| \geq O(1)$. The wave pressure $p^{(w)}$ matching to the inner solution (18) as $|\hat{\mathbf{x}}| \to 0$ is given by

$$\begin{aligned} p^{(w)}(\mathbf{x},t) = &-\rho_0 \frac{\dot{P}_0(t_r)}{r} - \rho_0 \partial_i \left[\frac{\dot{P}_i(t_r)}{r}\right] \\ &-\rho_0 \partial_i \partial_j \left[\frac{\dot{P}_{ij}(t_r)}{r}\right] \\ &-\rho_0 \partial_i \partial_j \partial_k \left[\frac{\dot{P}_{ijk}(t_r)}{r}\right] \\ &+\cdots\,, \end{aligned} \tag{19}$$

where $t_r = t - r/c$ is the retarded time. This is verified as follows.

Obviously, each term of (19) satisfies the wave equation. Matching of the two solutions $p^{(i)}$ and $p^{(w)}$ is carried out in an intermediate region. In terms of the inner variable defined by the normalization $\bar{x}_i \equiv x_i/l$ (and $\bar{r} = r/l$), both the outer variable $\hat{x}_i$ and intermediate variable ξ_i are given by

$$\hat{x}_i = M\bar{x}_i = M^{1-\alpha}\xi_i\,,\quad \xi_i = M^{\alpha}\bar{x}_i = (M^{\alpha}/l)\,x_i\,, \tag{20}$$

where α is a parameter in the range $0 < \alpha < 1$. Normalized retarded time is $\bar{t}_r \equiv t_r/\tau = \bar{t} - \hat{r} = \bar{t} - M^{1-\alpha}\xi$, where $\bar{t} = t/\tau$, $\hat{r} = r/\lambda$, and $\xi = M^{\alpha-1}\hat{r} = M^{\alpha}\bar{r}$. Using ξ, we have $\bar{r} = M^{-\alpha}\xi$ and $\hat{r} = M^{1-\alpha}\xi$. Thus in the limit $M \to 0$ with keeping ξ and ξ_i fixed (the intermediate limit), we obtain $\bar{r} \to \infty$ and $\hat{r} \to 0$. As an example we consider matching of the second-order term. The third term of the *inner* pressure (18) is written as

$$-\rho_0 \dot{P}^{(i)}_{ij}\,\partial_i\partial_j \frac{1}{r} = -\rho_0 \frac{M^{3\alpha}}{l^3}\dot{P}^{(i)}_{ij}(\bar{t})\,\frac{\partial^2}{\partial\xi_i\partial\xi_j}\frac{1}{\xi}\,,$$

whereas the third term of the outer *wave* pressure (19) is

$$-\rho_0 \frac{M^{3\alpha}}{l^3}\frac{\partial^2}{\partial\xi_i\partial\xi_j}\left[\frac{\dot{P}^{(w)}_{ij}(\bar{t} - M^{1-\alpha}\xi)}{\xi}\right] = -\rho_0 \frac{M^{3\alpha}}{l^3}\frac{\partial^2}{\partial\xi_i\partial\xi_j}\left[\frac{\dot{P}^{(w)}_{ij}(\bar{t})}{\xi} + \frac{1}{2}M^{2(1-\alpha)}\xi\Pi_{ij}(\bar{t}) + \cdots\right], \tag{21}$$

$$\Pi_{ij}(t) \equiv \frac{d^2}{dt^2}\dot{P}^{(w)}_{ij}(t)\,,$$

where the superscripts (i) and (w) are used to distinguish the functions in the two regions. It is found that both expressions have the same order of magnitude $M^{3\alpha}$ and we have $\dot{P}^{(w)}_{ij} = \dot{P}^{(i)}_{ij}$ in the intermediate limit as $M \to 0$. Crow [4] showed that the second term of the order $O(M^{3\alpha}M^{2(1-\alpha)}) = O(M^{2+\alpha})$ in the brackets [ ] on the RHS of (21) can be matched to the term in the next approximation (including an effect of compressibility, e.g., the term ρ_{tt}) of the inner expansion. Precisely speaking, an arbitrary term $C(\bar{t})\delta_{ij}$ can be added to $\dot{P}^{(w)}_{ij}(\bar{t})$ in the leading order matching. If so, in the next order $O(M^{2+\alpha})$ the second term in [ ] of RHS of (21) will include the additional term of the form $\ddot{C}\nabla^2(\xi/2) = \ddot{C}/\xi$. This arbitrariness drops out if we introduce a monopole term of the form $\dot{P}^{(w)}_0 = -(M^2/l^2)\ddot{C}(\bar{t})$ by the consistency argument [4]. Then the combined outer solution $\rho_0(M/l)^3\{\ddot{C}(\bar{t} - \hat{r})/\hat{r} - \hat{\nabla}^2[C(\bar{t} - \hat{r})/\hat{r}]\}$ vanishes identically. Matchings of the other terms are verified similarly. In particular, in the matching of the fourth terms, another arbitrariness in the dipole term comes in, but can be dropped out by the same reasoning.

The origin of the first *monopole* term of (19) is considered by Kambe [18] and Obermeier [19] (see also Ref. [7]). It is shown from the dynamical equation of motion (Navier-Stokes equation) that

$$P_0(t) = -\frac{5 - 3\gamma}{12\pi}\,\frac{1}{c^2}\,\dot{K}(t)\,,\quad K(t) = \tfrac{1}{2}\int v^2(\mathbf{y},t)\,d^3\mathbf{y}\,, \tag{22}$$

where K is the total kinetic energy and γ the ratio of specific heats. We assume that significant effect of the compressibility of the vortex motion appears only in this isotropic term due to the assumption of the compact source flow and $M \ll 1$, mentioned in the beginning. The rest factors $P_i\,, P_{ij}\,, P_{ijk}\,, \ldots$ of the multipole components of $p^{(w)}$ are given by $Q_i\,, Q_{ij}\,, Q_{ijk}\,, \ldots$ associated with the vorticity $\boldsymbol{\omega}$ as in Eqs. (13)–(15) and $R_i\,, R_{ij}\,, R_{ijk}\,, \ldots$ representing the influence of a solid body.

C. Far-field expression without external body

The expression (19) is the pressure of the acoustic wave generated by the vortex motion described by $\boldsymbol{\omega}(\mathbf{x},t)$. The second term of (19) represents *dipole* emission due to change of the total impulse $4\pi Q_i$ and/or presence of a solid body. In the present case of unbounded space where there exists neither solid body nor external force, the impulse $4\pi Q_i$ is conserved (see Sec. VI), and hence the dipole term disappears since the coefficient P_i is re-

lated to the force acting on the system [8,20]. The factors P_{ij} and P_{ijk} are given only by Q_{ij} and Q_{ijk}, respectively. The Q_{ij} terms are usually called *quadrupole.*

In the far-field where observations are made, the expansion is much simplified because, as $|\hat{\mathbf{x}}|$ becomes large, the space derivatives applied to r^{-1} in (19) become higher order of smallness than those applied to the functions of t_r as $\hat{r} \to \infty$. Neglecting those terms and retaining only the terms of $O(r^{-1})$, we obtain the far-field expression

$$p^{(f)}(\mathbf{x},t) = -\rho_0 \dot{P}_0^{(1)}(t_r)\frac{1}{r} - \frac{\rho_0}{c^2} Q_{ij}^{(3)}(t_r)\frac{x_i x_j}{r^3} + \frac{\rho_0}{c^3} Q_{ijk}^{(4)}(t_r)\frac{x_i x_j x_k}{r^4} + \cdots , \tag{23}$$

where superscript (n) denotes the nth time derivative. The first term is isotropic and is related to the rate of energy dissipation $\dot{\epsilon} = -\ddot{K}$. This is written as ($\gamma = 7/5$ for the air)

$$A_0(t_r) \equiv -\frac{\rho_0}{r} P_0^{(1)}(t_r) = \frac{\ddot{K}}{15\pi c^2 r} = -\frac{\dot{\epsilon}}{15\pi c^2 r} . \tag{24}$$

Here we have retained up to the Q_{ijk} terms, i.e., the third-order moments of the vorticity $\boldsymbol{\omega}$ [see (15)]. This is because in the experimental observation these components have been found to be significant, as described below.

D. Oblique collision

Consider a problem that the initial state is given as follows. Two vortex rings are set to move along the paths intersecting at right angles at the origin and collide with one another. The bisecting straight line between the two paths of the vortex center is taken as the polar axis $\theta = 0$ (along the x_3 axis) of the spherical coordinate system (Fig. 1). The plane perpendicular to the x_3 axis is the (x_1, x_2) plane on which $\theta = \pi/2$. There are two symmetry planes including the x_3 axis: one includes the trajectories of the vortex centers which is defined as the (x_2, x_3) plane and the plane (x_1, x_3) perpendicular to it is also a symmetry plane which bisects the two trajectories. The plane $\phi = 0$ is taken along the positive x_1 axis. Thus the two vortex rings (centers) move toward the origin along the direction of the angles $(\theta, \phi) = (\pi/4, \pi/2)$ and $(\pi/4, 3\pi/2)$ before colliding interaction. From the geometrical arrangement just mentioned, the acoustic pressure $p(\theta, \phi, t)$ is characterized by the symmetry

$$p(\theta, -\phi, t) = p(\theta, \phi, t) , \quad p(\theta, \phi + \pi, t) = p(\theta, \phi, t) . \tag{25}$$

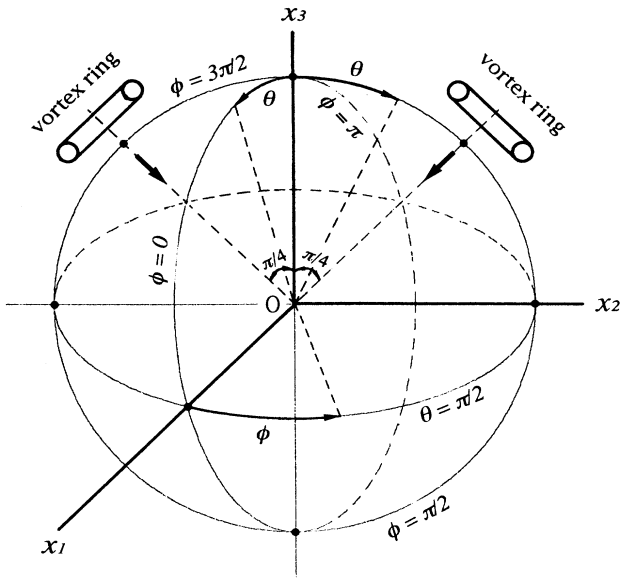

FIG. 1. Setup of the collision of two vortex rings and coordinate systems.

The formula (23) is rewritten by using the spherical polar coordinates (r, θ, ϕ): $x_1 = r\sin(\theta)\cos\phi$, $x_2 = r\sin(\theta)\sin\phi$, and $x_3 = r\cos\theta$. Then the nth order form, like the expression $F_2 = -Q_{ij}^{(3)} x_i x_j / r^2$ for $n = 2$ or $F_3 = Q_{ijk}^{(4)} x_i x_j x_k / r^3$ for $n = 3$, can be represented in terms of the nth order (or lower-order) spherical harmonics,

$$P_n^0(\zeta) , \quad P_n^1(\zeta)\,(\cos\phi,\ \sin\phi) , \ldots , \quad P_n^n(\zeta)\,(\cos(n\phi),\ \sin(n\phi)) ,$$

where $P_n^0(\zeta)$ and $P_n^k(\zeta)$ are the Legendre polynomials ($k = 1, \ldots, n$) and $\zeta = \cos\theta$. In fact, we have

$$\begin{aligned} F_2 = {} & \tfrac{1}{3}(Q_{11}^{(3)} + Q_{22}^{(3)} - 2Q_{33}^{(3)})P_2^0 + \tfrac{1}{6}(-Q_{11}^{(3)} + Q_{22}^{(3)})P_2^2\cos(2\phi) \\ & -\tfrac{1}{3}(Q_{13}^{(3)} + Q_{31}^{(3)})P_2^1\cos\phi - \tfrac{1}{3}(Q_{23}^{(3)} + Q_{32}^{(3)})P_2^1\sin\phi - \tfrac{1}{6}(Q_{12}^{(3)} + Q_{21}^{(3)})P_2^2\sin(2\phi) . \end{aligned} \tag{26}$$

Similarly, the third-order form F_3 is given as follows:

$$\begin{aligned} F_3 = {} & \tfrac{1}{5}(2Q_{333}^{(4)} - \tilde{Q}_{113}^{(4)} - \tilde{Q}_{223}^{(4)})P_3^0 + \tfrac{1}{30}(\tilde{Q}_{113}^{(4)} - \tilde{Q}_{223}^{(4)})P_3^2\cos(2\phi) \\ & +[\text{linear combination of } \{P_3^1\cos\phi,\ P_3^1\sin\phi,\ P_3^2\sin 2\phi,\ P_3^3\cos 3\phi \text{ and } P_3^3\sin 3\phi\}] , \end{aligned} \tag{27}$$

where only the terms to be used later are written explicitly, and the tilde symbol denotes $\tilde{Q}_{113} = Q_{113} + Q_{131} + Q_{311}$, etc. By the relations (16), the coefficients of P_2^0, P_3^0, and P_3^2 are reduced to

$$\tfrac{1}{3}(Q_{11}^{(3)} + Q_{22}^{(3)} - 2Q_{33}^{(3)}) = -Q_{33}^{(3)} , \tag{28a}$$

$$\tfrac{1}{5}(2Q_{333}^{(4)} - \tilde{Q}_{113}^{(4)} - \tilde{Q}_{223}^{(4)}) = Q_{333}^{(4)} - (1/5)\,Q_{3kk}^{(4)} , \tag{28b}$$

$$(\tilde{Q}^{(4)}_{113} - \tilde{Q}^{(4)}_{223}) = Q^{(4)}_{311} - Q^{(4)}_{322} + 2(Q^{(4)}_{113} - Q^{(4)}_{223}) \ . \quad (28c)$$

In view of the symmetry (25), the terms of the second line of Eqs. (26) and (27) must disappear. Thus the pressure (23) with the symmetry (25) suggests the following form:

$$\begin{aligned} p(\theta,\phi,t) = {} & A_0(t) + A_1(t)P_2^0(\cos\theta) \\ & + A_2(t)P_2^2(\cos\theta)\cos(2\phi) \\ & + B_1(t)P_3^0(\cos\theta) + B_2(t)P_3^2(\cos\theta)\cos(2\phi) \ , \end{aligned} \quad (29)$$

if the pressure is observed at the stations $(r_{\rm obs}, \theta, \phi)$ on a spherial surface of a fixed radius $r_{\rm obs}$ centered at the origin. Thus it is found that the far-field acoustic pressure is represented in terms of the five normal modes with five coefficient functions of time,

$$\mathbf{A} = (A_0(t),\ A_1(t),\ A_2(t),\ B_1(t),\ B_2(t)) \ .$$

This result is useful for the analysis of the observed signals. Here the Legendre functions are $P_2^0=(1/2)(3\cos^2\theta-1)$, $P_2^2=3\sin^2\theta$, $P_3^0=(1/2)(5\cos^3\theta-3\cos\theta)$, and $P_3^2=15(\cos\theta-\cos^3\theta)$.

Considering Eqs. (23) and (26)–(29), the main mode coefficients are written in terms of tensor coefficients as

$$A_1(t) = -\frac{\rho_0}{c^2 r_{\rm obs}} Q^{(3)}_{33}(t) \ , \quad (30a)$$

$$A_2(t) = -\frac{\rho_0}{6c^2 r_{\rm obs}} [Q^{(3)}_{11}(t) - Q^{(3)}_{22}(t)] \ , \quad (30b)$$

$$B_1(t) = \frac{\rho_0}{c^3 r_{\rm obs}} [Q^{(4)}_{333}(t) - (1/5)Q^{(4)}_{3kk}(t)] \ , \quad (30c)$$

$$B_2(t) = \frac{\rho_0}{c^3 r_{\rm obs}} \frac{1}{30} [\tilde{Q}^{(4)}_{113}(t) - \tilde{Q}^{(4)}_{223}(t)] \ , \quad (30d)$$

where $A_0(t)$ is given by (24). Note that the retarded time t_r is replaced by t for simplicity since r/c does not change the profiles. The right-hand sides can be estimated by the numerical simulation described in Sec. IV. Thus the expressions (29) and (30) provide the basis of comparison between the observation and the numerical simulation.

III. EXPERIMENT

A. Experimental setup and procedure

Two vortex rings are generated experimentally by using a shock tube. The experimental method is essentially the same as that described in Ref. [7]. The shock wave formed in the tube is bifurcated into two polyethylene pipes. The pipes are connected to the end of the shock tube on one side and to two straight nozzles in a cubic anechoic chamber of inner size 1.8 m on the other side. The two straight nozzles (of length 750 mm and circular section of the inner diameter 6 mm) are placed at right angles. The central axes of the nozzles intersect at the center O of the anechoic chamber, and the distance between the intersecting point O and the exit end of each nozzle was 41 mm. The shock waves transmitting through the pipes emerge out of the two nozzle ends into the air at a room condition (1 atm, 21.0 °C, and $c = 344.0$ m/s). Two vortex rings are formed simultaneously at the two exits by the shock impulse. They approach to each other with their self-induced motion and perform almost 90° collision. The collision process of the vortex cores was observed by means of a photosensor and the shadowgraph technique. The signals from the photosensor are recorded in a microprocessor. These signals are averaged over ten or five measurements.

The acoustic waves emitted by the 90° collision are received simultaneously by four 1/2-inch microphones (Brüel & Kjaer type 4165). The acoustic pressures were detected at 102 different angular positions on the three great circles of radius $r_{\rm obs} = 620$ mm (with their centers at the origin) on the three orthogonal planes: (1) $\phi = (\pi/2,\ 3\pi/2)$, (2) $\phi = (0,\ \pi)$, and (3) $\theta = \pi/2$. Recording of the acoustic signal is triggered by the shock signal from a pressure transducer mounted on one of the nozzles. The raw acoustic signal of a single event is stored in the form of a digital data set of 1000 words in the microprocessor through an analog-to-digital converter. The wave signals associated with the interaction of the vortex rings are extracted later by eliminating irrelevant noise from the recorded signals by the same method described in Ref. [21]. Only average profiles (taken over ten such sets of data) are considered below.

B. Experimental results

1. Vortex motion

The trajectories of the vortex cores in the (x_2, x_3) plane observed by the photosensor are shown in Fig. 2, where the position Z of each vortex ring denotes the distance from the end of each nozzle. The passage time T corresponding to the vortex position Z was also measured.

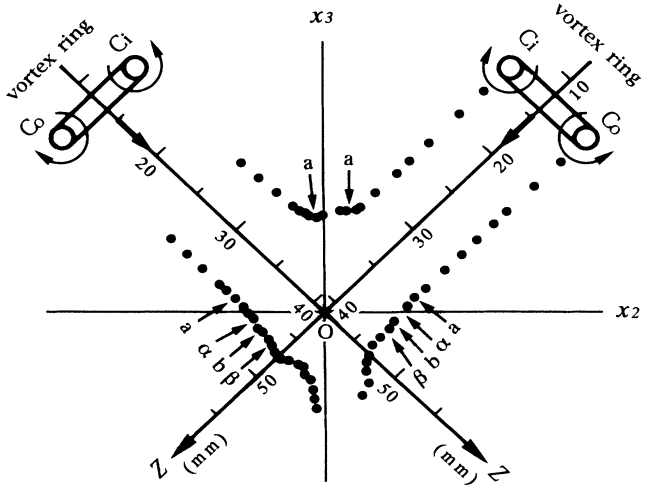

FIG. 2. Observed trajectories of the vortex cores in the (x_2, x_3) plane with C_i denoting the core inside and C_o the core outside. The coordinate Z is the distance (mm) from the end of each nozzle. The arrows with a, b, α, and β mark the positions corresponding to those in Figs. 3 and 7.

The measurement was made for the cores C_o (outside) and C_i (inside) of each vortex shown in Fig. 2. Motion of the core of a single isolated vortex ring was also examined. These results are shown in Fig. 3, where the circles, squares, and triangles show respective positions. The origin of the passage time T is taken at the same origin of the acoustic measurement. These data of the position Z are represented in terms of a polynomial of the third order with respect to T, as shown by the solid lines in the figure. The three lines show good agreement up to the distance Z=25 mm (or the time T = 2.8 ms). It is found from these figures that the two vortex rings move along the two straight paths intersecting at right angles like steady vortex rings with the diameter $D=2R_0$=9.4 mm and velocity U=27.3 m/s up to the distance of about 25 mm, where R_0=4.7 mm denotes the ring radius of the initial state. Hence the interaction of each vortex is weak in the initial phase. After that, two vortex rings interact each other strongly and the two vortex cores denoted as C_i (squares of Fig. 3) come into contact. The signal of the vortex core C_i by the photosensor failed to be observed at around 34 mm. On the other hand, the speed and the size of the side C_o do not change significantly up to the distance about 35 mm (or time T=3.3 ms), and these are the same as the single vortex ring (triangles of Fig. 3). The upper abscissa in Fig. 3 denotes the time t (ms) of the acoustic measurement, and t is related to the vortex passage time T (ms) by $t = T + r_{obs}/c$, where r_{obs}/c=1.80 ms is the retarded time.

Typical parameters of the present system are summarized as follows: l=4.7 mm (R_0), u=27 m/s (U), τ= 0.17 ms, and M=0.08. Then we have the typical wave scale $\lambda=c\tau$=58 mm with r_{obs}/λ=10.7.

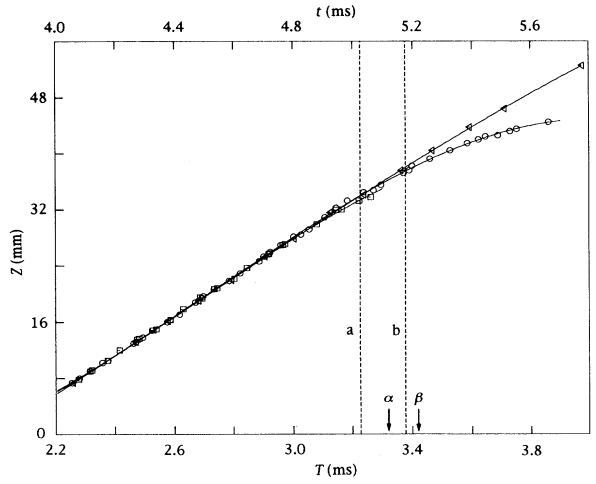

FIG. 3. Observed vortex position Z is plotted against the time T of passage over the photosensor (lower abscissa) and the corresponding time t of the wave recording (upper abscissa): circles (core C_o), squares (core C_i), and triangles (a single vortex). The solid curves are the polynomial representation $Z = \sum_{n=0}^{3} z_n T^n$ with the coefficients z_n determined to fit the measurement. The broken lines a and b denote the times T = 3.23 and 3.38 ms, corresponding to those of Figs. 2 and 7.

2. *Emitted sound*

Figures 4, 5, and 6 show the average profiles (bold lines) of the acoustic pressure at every angle $\pi/6$ of θ or ϕ (the measurement having been made at every $\pi/18$ =10°) on the great circles in the three orthogonal planes: (x_2, x_3), (x_1, x_3), and (x_1, x_2) planes, respectively. Light solid lines are the rms error of the average pressure at each time point. The geometry of the setup described in Sec. II D suggests that the acoustic pressure $p(\theta, \phi, t)$ is characterized by the symmetry (25), which is consistent with the observed data. In fact, the acoustic pressure detected in the plane $\theta = \pi/2$ was expanded into Fourier series with respect to the angle ϕ, and it has been found that the Fourier coefficients of $\sin(m\phi)$ and $\cos(m\phi)$ were all insignificant except those of $\cos(2\phi)$ and 1. In the Fourier decomposition with respect to the angle θ in the plane (x_2, x_3), the component of $\sin(2\theta)$ has been found, which is considered to be caused by asymmetrical vortex motion (e.g., tilting of the x_3 axis as seen in Fig. 2), but its amplitude is relatively small compared to the components of $\cos(m\theta)$ (m = 0–3). Hence we neglect this asymmetrical component and assume that the detected acoustic pressure is expressed by (29) where higher-order terms are neglected since the observed Fourier coefficients of those terms are not significant. The amplitudes of the main modes $\mathbf{A} = (A_0, A_1, A_2, B_1, B_2)$ in (29) can be determined as a function of time with the least squares method by using the data measured in two different orthogonal planes in the following way. The pressure signals observed at 36 angular stations of θ along the observation circle $r = r_{obs}$ in the plane (x_2, x_3) are expressed by Eq. (29) in which $\cos(2\phi)$=−1. Hence we obtain 36 simultaneous linear equations for the five amplitudes of $\mathbf{A}$ at each time point. Similarly we obtain another 36 linear equations for the same unknown amplitudes of $\mathbf{A}$ from the data observed in the plane (x_1, x_3) at which $\cos(2\phi)$=1. From these 72 algebraic equations, the amplitudes $\mathbf{A} = (A_0, \ldots, B_2)$

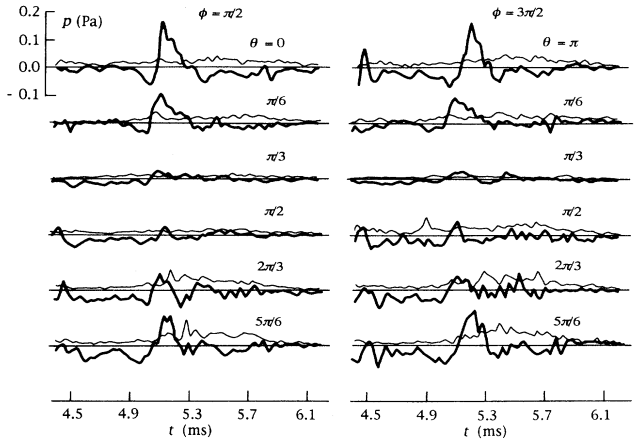

FIG. 4. Average profiles (bold curves) of the acoustic pressure observed at 12 angular positions of θ in the (x_2, x_3) plane ($\phi = \pi/2$, $3\pi/2$ and r_{obs} = 620 mm). The light curves are the rms error of the average curve at each time point.

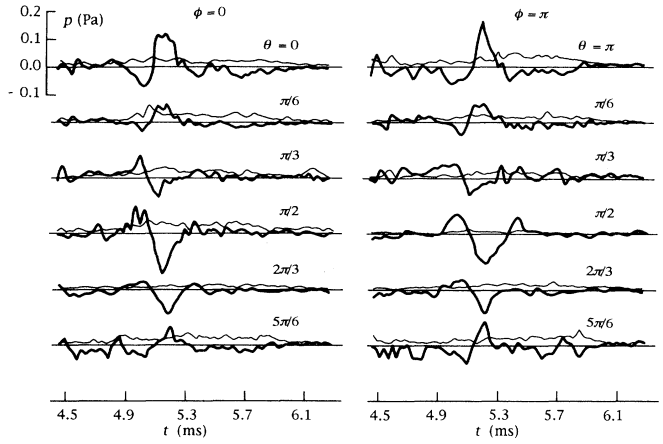

FIG. 5. Average profiles (bold curves) of the acoustic pressure observed at 12 angular positions of θ in the (x_1, x_3) plane ($\phi = 0$, π and $r_{\rm obs} = 620$ mm). The light curves are the rms error of the average curve at each time point.

are determined by the least squares method at each time point. The profiles thus obtained are shown in Figure 7. The ordinate marked on the left-hand side denotes the scale in the unit Pa, while the one on the right-hand side denotes the scale of the modes A_0, A_1, and A_2 normalized by $\rho_0 R_0 U^4/(c^2 r_{\rm obs})$ and the modes B_1 and B_2 normalized by $\rho_0 R_0 U^5/(c^3 r_{\rm obs})$. The upper abscissa denotes the time scale normalized by R_0/U, where the origin of the normalized time is taken at the time t=5.178 ms marked by the broken line b. These dimensionless quantities $[\tilde{A}_0, \tilde{A}_1, \tilde{A}_2, \tilde{B}_1, \tilde{B}_2]$ and $\tilde{t}$ are compared with the results of the numerical simulation (Fig. 12).

It is found that the monopole amplitude $A_0(t)$ is small, whereas the two quadrupole amplitudes $A_1(t)$ and $A_2(t)$ are substantial. The first quadrupole mode $P_2^0(\cos\theta)$=$(3\cos^2\theta - 1)/2$ is axisymmetric and the second mode $P_2^2(\cos\theta)\cos(2\phi)$=$3\sin^2(\theta)\cos(2\phi)$ would be

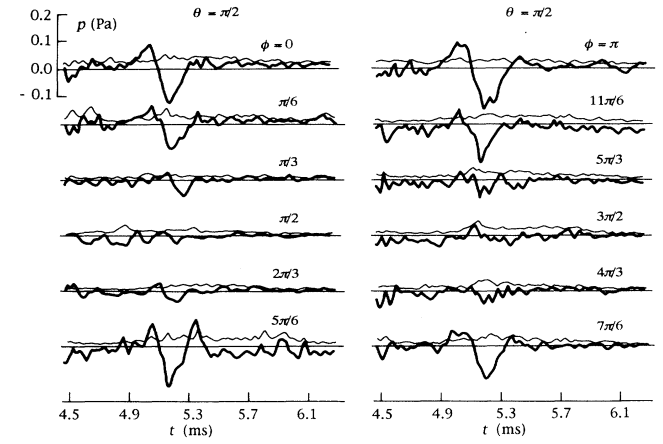

FIG. 6. Average profiles (bold curves) of the acoustic pressure observed at 12 angular positions of ϕ in the (x_1, x_2) plane ($\theta = \pi/2$ and $r_{\rm obs} = 620$ mm). The light curves are the rms error of the average curve at each time point.

related to an anisotropy in the (x_1, x_2) plane as inferred from its coefficient $-Q_{11}^{(3)} + Q_{22}^{(3)}$ of (26). The effect of these two quadrupoles on the acoustic pressure is of the same order. In fact, the larger amplitude of $A_1(t)$ is almost compensated by the smaller modal amplitude of P_2^0 as compared with the pair $[A_2(t), P_2^2]$. The third-order mode $B_1(t)$ is significant. Two broken lines a and b in Fig. 7 denote the times of the sound which indicate, respectively, the minimum and maximum amplitudes of the quadrupole mode A_1 (or the maximum and the minimum of the mode A_2). The amplitude of the mode B_1 takes the maximum and minimum values at the times 5.124 ms (α) and 5.223 ms (β) marked by arrows. These times a, b, α, and β are also shown in Fig. 3, and the vortex ring at these times is located at the position of the arrows a, b, α, or β marked in Fig. 2, respectively.

Figures 8, 9, and 10 show the instantaneous directional distributions of the acoustic pressure at six times measured on each great circle in the planes ϕ=$(\pi/2, 3\pi/2)$, ϕ =$(0, \pi)$, and θ=$\pi/2$, respectively, in which the radial length from the origin represents the magnitude of pressure with a linear scale. The single and double circles denote positive and negative values of the observed pressure, respectively. The thin solid curves show the quadrupolar distribution as calculated with the sum of two quadrupole components $A_1(t)[3\cos^2(\theta) - 1]/2$ and $A_2(t)3\sin^2(\theta)\cos(2\phi)$, using the amplitudes $A_1(t)$ and

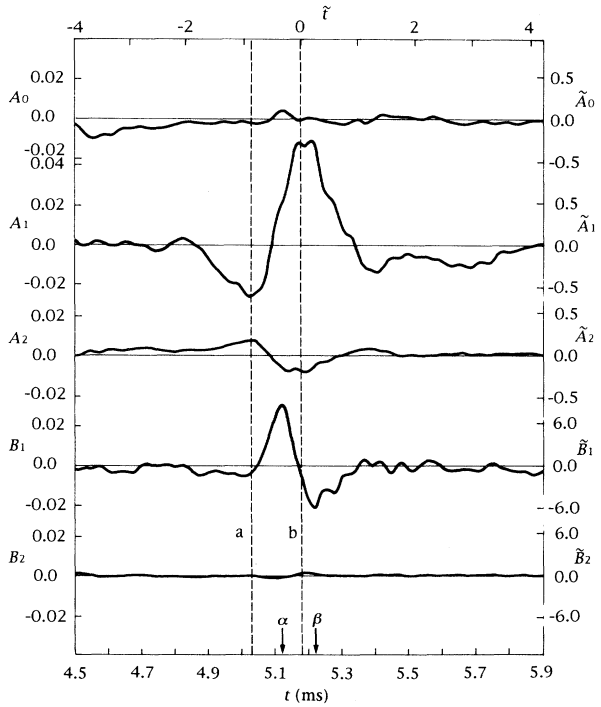

FIG. 7. Observed amplitudes of five dominant wave modes of Eq. (29) plotted against the time t (ms) with the origin fixed by the shock signal. The left and right ordinates denote the pressure scale in the unit Pa and the dimensionless scale, respectively. The upper time scale is dimensionless with the origin at the time b. The marked times are (a, b)=(5.031, 5.178) ms and (α, β)=(5.124, 5.223) ms.

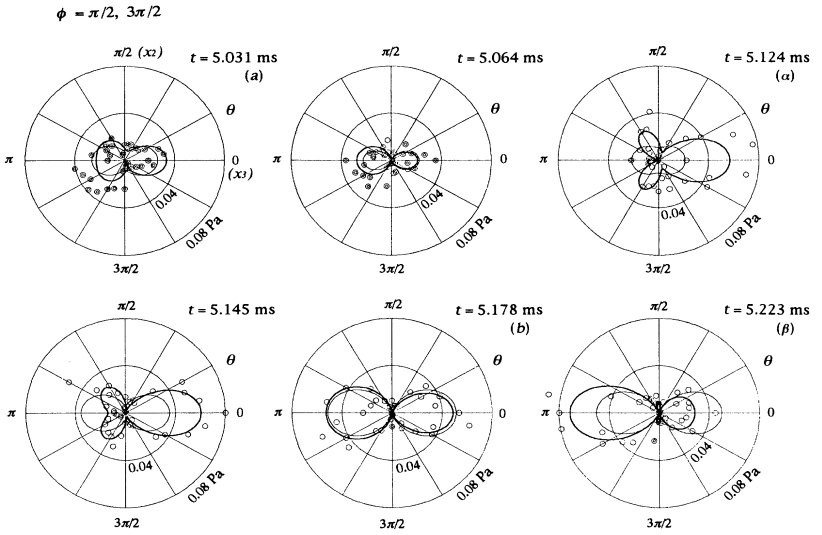

FIG. 8. Polar diagram of the pressure at six times corresponding to the signals of Fig. 4 [measured in (x_2, x_3) plane] and the curves of Fig. 7. The labels a, b, α, and β refer to positions marked in Figs. 3 and 7. The single and double circles denote positive and negative values of the observed pressure. The thick solid curves show the pressure of (29) with all the amplitudes $(A_0, \ldots, B_2)$ at the time shown, and the thin curves are the quadrupolar component from A_1 and A_2.

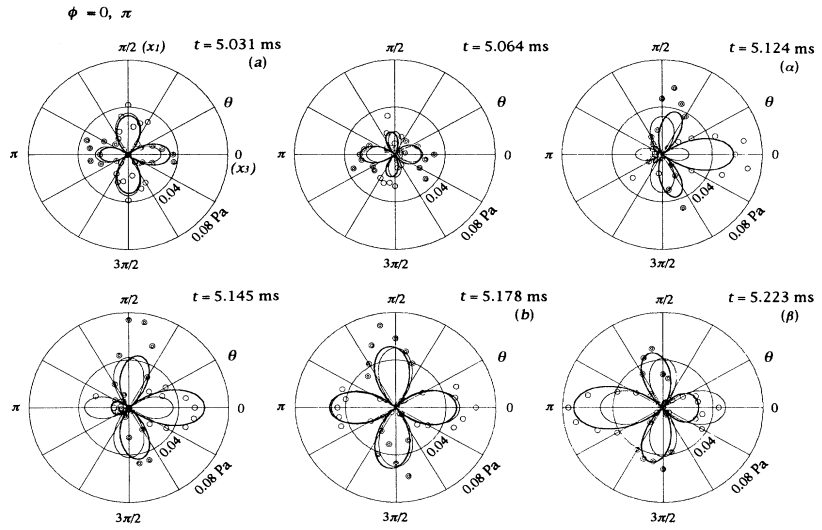

FIG. 9. Polar diagram of the pressure at six times corresponding to the signals of Fig. 5 [measured in (x_1, x_3) plane] and the curves of Fig. 7. The curves and marks are as in Fig. 8.

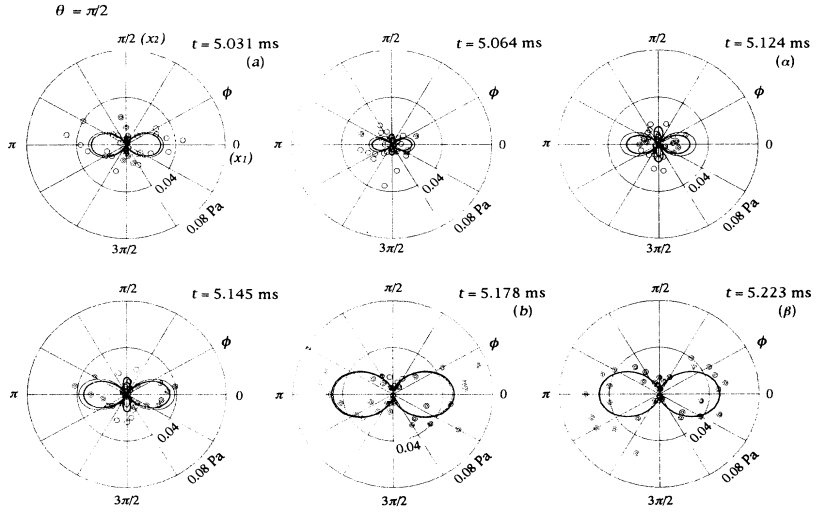

FIG. 10. Polar diagram of the pressure at six times corresponding to the signals of Fig. 6 [measured in (x_1, x_2) plane] and the curves of Fig. 7. The curves and marks are as in Fig. 8.

$A_2(t)$ in Fig. 7. The thick solid lines represent the distribution calculated with the form (29), using the components $A_0(t)$, $A_1(t)$, $A_2(t)$, $B_1(t)$, and $B_2(t)$. The difference of the directional distribution between Figs. 8 and 9 lies only on the value of the angle ϕ, i.e., $\cos(2\phi)=-1$ for Fig. 8 and 1 for Fig. 9. The effect of the amplitude $B_1(t)$ is significant at later times. The directional distributions at 5.031 ms, 5.178 ms, 5.124 ms, and 5.223 ms in these figures represent those at the times a, b, α, and β in Fig. 7, respectively.

IV. NUMERICAL SIMULATION

A. Methods and conditions of numerical simulation

Numerical simulation of collision of two vortex rings was carried out for the parallel initial setup and also for several initial angles in order to see the mechanism of vortex reconnection [22]. The vortex collision at right angles, which corresponds to our experiment described in the previous section, has been simulated in detail (Fig. 11)

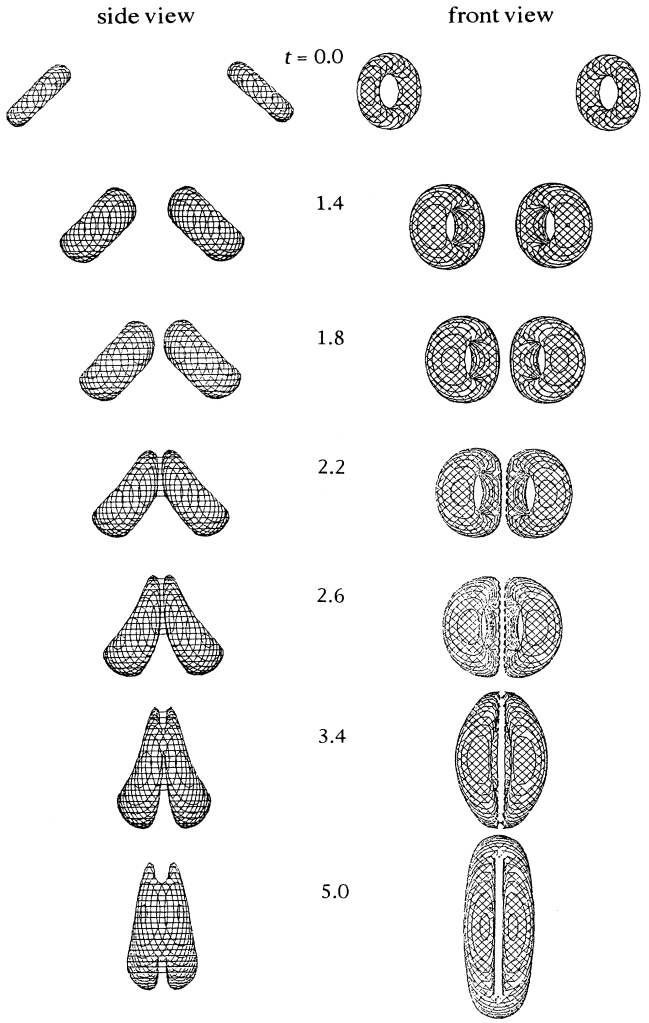

FIG. 11. Computed side views and front views of the collision of two vortex rings at right angles. The illustrations are the isovorticity surface of magnitude ($|\omega|$) at the level of 0.40 of the maximum vorticity at each instant.

using the same computational methods in order to estimate the acoustic emission by the vortex interaction in which the antiparallel configuration of vortex lines at the inner part is susceptible to reconnection by the vortex motion itself. The initial vortex rings are set at such a sufficient distance that enables us to see both a translational phase and an interacting phase.

The Navier-Stokes equation (3) is solved numerically together with the continuity equation (4) by the pseudospectral method on $N^3=64^3$ grid points. Periodic boundary conditions are assumed with the period 2π in the three orthogonal directions. The alias error is eliminated by a shifted Fourier transform (see Ref. [23]). The Runge-Kutta-Gill scheme is used for the time marching with the time increment $\triangle t=0.05$.

Initially, two vortex rings are set with $d = 3.65$, d being the distance between their centers. The vorticity is distributed along the circular center line of each vortex with Gaussian core,

$$\omega(\sigma) = \omega_0 \exp[-(\sigma/a)^2],$$

where $a=0.20$, $\omega_0=23.8$, and σ is the distance from the center lines. Vorticity fields below 1% of its maximum value (ω_0) are set to be zero. In Table I are listed the parameters used in the present numerical simulation, where $D = 2R_0$ and ρ_0 are the diameter of vortex rings and density of fluid, respectively. The circulation of the vortex tube is $\Gamma = \pi a^2 \omega_0 = 2.88$ and the translational velocity U of the vortex rings is estimated by Saffman's formula for a thin vortex ring [24],

$$U = \frac{2.88}{4\pi \times 0.49}\left[\log_e\left(\frac{8 \times 0.49}{0.20}\right) - 0.558\right] = 1.13 \ .$$

B. Estimation of the vortex sound

The Reynolds number of the present numerical simulation is much smaller in magnitude than that of the experiment (see Table I) and hence the effect of viscous diffusion would be considerably larger. The calculated coefficients of vortex sound using the data of the simulation would contain both effects of the viscous diffusion of vorticity and the interaction of two vortex rings. It is thus desirable to separate these two effects in order to estimate the main-mode coefficients associated with the vortex interaction which is considered to be dominant in the experiment.

In order to remove the effect of viscous diffusion, we

TABLE I. Parameters of the computer simulation and the experiment.

Parameter	Simulation	Experiment
$D = 2R_0$	0.98	9.4 mm
ρ	1.0	1.2×10^{-3} kg/m^3
ν	0.01	1.5×10^{-5} m^2/sec
U	1.13	27.3 m/sec
$M = U/c$		0.08
$Re = UR_0/\nu$	55	8550

also simulated the motion of a single isolated vortex ring with the same initial condition as the one of the two vortex rings in the collision case. (Note that in the experiment we also removed the acoustic waves prior to the interaction.) Then we construct the vorticity field by superposing the field of its mirror symmetry on that of this single ring, that is, two vortex rings go through merely without interaction. The difference of acoustic waves calculated from the realistic simulation field (with the interaction) and this imaginary field (without interaction) is considered to give a rough estimate of the acoustic waves caused by the vortex interaction.

Wave profiles of the vortex sound are calculated from the field variables of the vortex motion. The isotropic component is proportional to the time derivative of the energy dissipation rate ϵ [see Eq. (24)], and quadrupole components and higher modes are related to the time development of moments of the vorticity distribution. Using the data from the numerical simulation, we can obtain the tensor coefficients $Q_{ij}(t)$ and $Q_{ijk}(t)$ defined in (14) and (15). The spatial integrations of these moments are carried out over the whole space of $(2\pi)^3$ periodic box by using the real data on 128^3 grid points, which are made from the 64^3 Fourier data. That is, the vorticity outside of this periodic box is set to be zero and the real data are interpolated by Fourier functions. The main-mode coefficients $\mathbf{A} = (A_0, \ldots, B_2)$ of the acoustic pressure in (29) are calculated by using Eq. (24) and Eqs. (30a)–(30d).

Thus, the mode amplitudes of $\mathbf{A}$ are found in the numerical simulation by removing the viscous diffusion effect as mentioned above and normalized by using the radius R_0 and velocity U. The time is normalized as tU/R_0 and the tensor coefficients are normalized as $Q_{ij}^{(3)}/(R_0U^4)$ and $Q_{ijk}^{(4)}/(R_0U^5)$. In Fig. 12 these dimensionless quantities $(\tilde{A}_0, \ldots, \tilde{B}_2)$ are shown as the function of the dimensionless time $\tilde{t}$ for comparison with the experimental amplitudes with the scales on the right-hand side of Fig. 7 (the origin of $\tilde{t}$ being chosen near the peak position of $\tilde{A}_1$, which is $t = 2.5$). The time develoments of the tensor coefficients are interpolated by a B-spline function to calculate their time derivatives and the curves are smoothed out. Figure 13 compares the rate of energy dissipation $\epsilon(t)$ for the present case with twice that of a single isolated vortex ring $\epsilon_0(t)$. The difference $\Delta\epsilon(t) = \epsilon(t) - 2\epsilon_0(t)$ is considered to be the rate enhanced by the vortex interaction.

The normalized vortex sound is defined as

$$\tilde{p}(\theta,\phi,t) = \tilde{A}_0(t) + \tilde{A}_1(t)P_2^0(\cos\theta) + \tilde{A}_2(t)P_2^2(\cos\theta)\cos(2\phi) + M[\tilde{B}_1(t)P_3^0(\cos\theta) + \tilde{B}_2(t)P_3^2(\cos\theta)\cos(2\phi)] , \quad (31)$$

obtained by dividing Eq. (29) with $(\rho_0 RU^4)/c^2 r_{\rm obs}$, where $M{=}U/c$ is the Mach number and set at the exper-

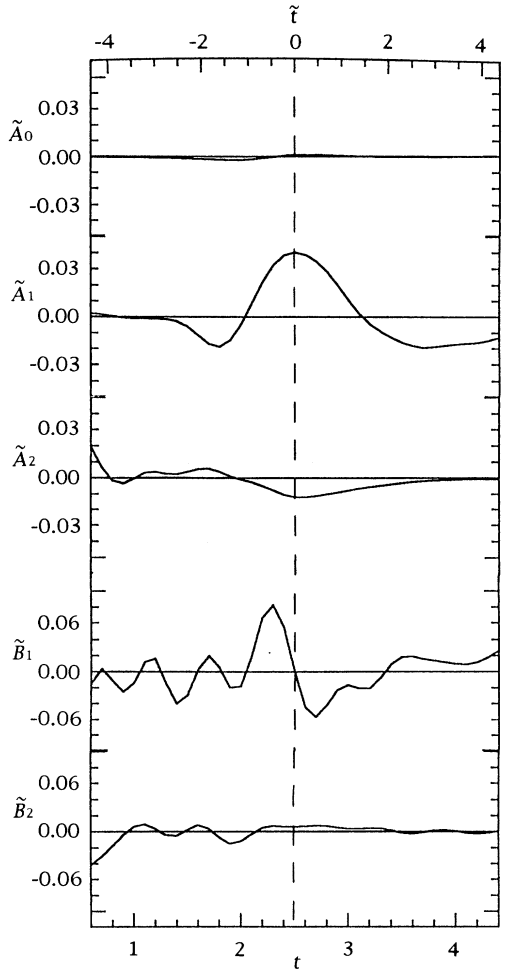

FIG. 12. Calculated mode amplitudes $(\tilde{A}_0, \ldots, \tilde{B}_2)$ from the numerical simulation. The lower time is the time t in the simulation, and the upper one is the time $\tilde{t}$ normalized by R_0/U with the origin at the time b.

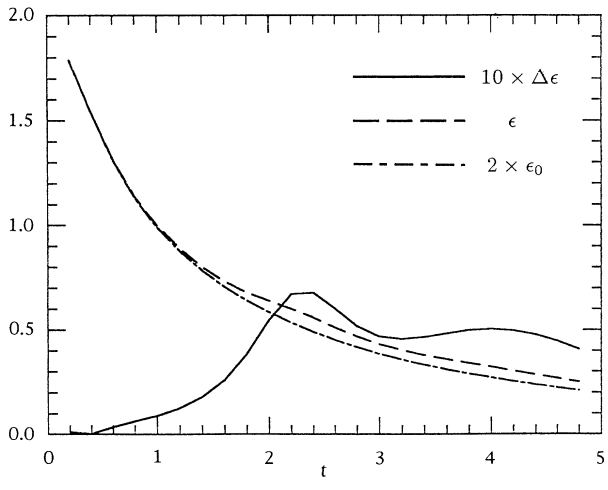

FIG. 13. Time developments of the rate of energy dissipation ϵ (broken line), twice that of a single vortex ring ϵ_0 (dot-dash line), and their difference $\Delta\epsilon$ (solid line) multiplied by 10, from the computer simulation.

imental value $M=0.08$. The order of the time derivative in the amplitudes $A_1(t)$ and $A_2(t)$ is the third of $Q_{ij}(t)$, whereas that of $B_1(t)$ and $B_2(t)$ is the fourth of $Q_{ijk}(t)$. In view of the small multiplying factor M to $\tilde{B}_1(t)$ and $\tilde{B}_2(t)$, the third-order modes P_3^0 and P_3^2 become significant only when time variation of $\omega(\mathbf{y},t)$ is very rapid, namely when an energetic motion is excited.

In the numerical simulation itself there is no acoustic wave because of the incompressibility condition imposed to the computation. However, in the theory of the Sec. II taking account of the fluid compressibility, the wave profile can be calculated by using the vorticity obtained from the incompressible simulation in an asymptotic sense as $M \to 0$. Equation (31) represents the time variation of the wave pattern.

V. COMPARISON OF THE EXPERIMENTAL OBSERVATION AND THE NUMERICAL SIMULATION

The behaviors of the mode amplitudes of Figs. 7 and 12 are qualitatively similar, but quantitatively different. This is considered to be due to the difference of the Reynolds numbers, i.e., the experimental Reynolds number is two orders of magnitude higher than the computational Reynolds number (Table I). Although the dimensionless time scale of the numerical curves is larger, about 1.7 times of the experimental ones, there is coincidence in the qualitative property that the time interval of the positive peak of the amplitude B_1 lies in the interval between the two lines a and b, i.e., corresponding to the minimum and maximum of the amplitude A_1 in Figs. 7 and 12.

Remarkable similarity is found for the time evolution of the vortex structures. To compare with the computed diagrams of Fig. 11, shadowgraphs of the oblique collision are shown in Fig. 14 (side views) and Fig. 15 (rear views), in which density inhomogeneity is taken in pictures with the optical effect integrated along the line of sight. The cores of the vortex rings are seen as thin filaments at the front of starting jets issuing from two nozzles set at right angles in Fig. 14(a) and as deformed closed curves in Fig. 15(a). Figures 15(b)–15(d) are the shadowgraph illustration of the process of reconnection of the vortices and corresponding side views are shown in Figs. 14(b)–14(d). These pictures are taken at different experimental events, not sequential in a single event. The vortex speed is higher in this optical observation ($U=81$ m/s, $R_0=4.5$ mm, $Re=2.4\times10^4$) than that in the previous acoustical observation. Owing to the higher speed, traces of wave generation are seen in the shadowgraphs, say Figs. 14(c) or 15(c). Morphological similarity between the computed vortex structures and the optical ones is apparent in the Figs. 11, 14, and 15.

Quantitatively speaking, the amplitudes of the dimensionless modes $\tilde{A}_1$ and $\tilde{A}_2$ in the experiment are about 25 times of those of the simulation, and the observed mode $\tilde{B}_1$ is about 125 times of the simulation. In the real scale the observed B_1 is the same order as the observed A_1 or A_2, but the numerical mode B_1 is about one-fifth of

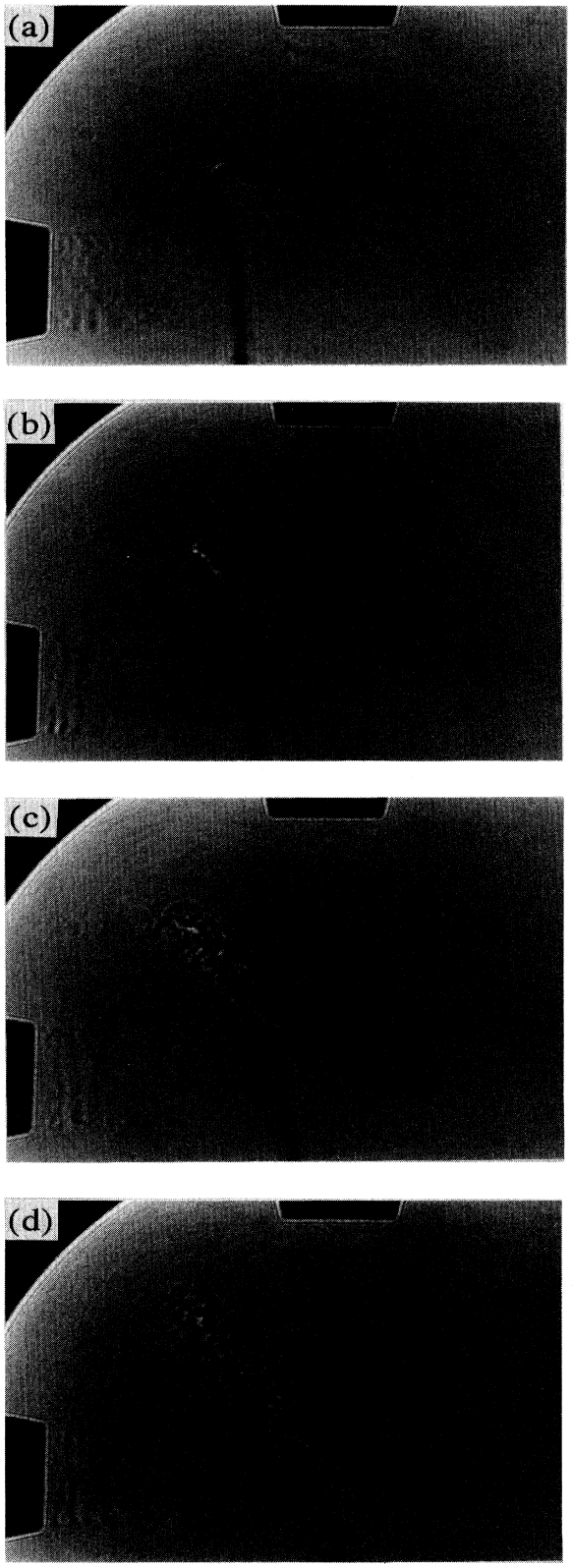

FIG. 14. Shadowgraphs of the side view of the collision of two vortex rings at a higher vortex speed than that of the acoustic measurement: (a) 0 μs, (b) 20 μs, (c) 40 μs, and (d) 60 μs [relative time from the instant (a)].

the numerical mode A_1 or A_2. Therefore there is little contribution of the mode B_1 to the computed directional distribution of the wave. Accordingly computational diagrams corresponding to Figs. 8–10 have approximate up-down symmetry (with respect to the x_3 axis), which is represented mainly by the two quadupoles $A_1(t)P_2^0(\cos\theta)$ and $A_2(t)P_2^2(\cos\theta)\cos(2\phi)$. The larger time scale in the computation (due to the larger viscosity effect) results in the smaller amplitudes because the amplitudes are determined by time derivatives. The numerical simulation at the Reynolds number as high as the experimental one has not been performed so far, unfortunately, because of the limited computer power. Therefore at present we have no estimate of the viscosity dependence of the mode amplitudes and also that of the vortex interaction. Note that the results of the numerical simulation by Ref. [25] for the head-on collision of two vortex rings imply that the computed profile obtained at lower Reynolds numbers get nearer to that of the experiment at a higher Reynolds number when the Reynolds number of the simulation is increased.

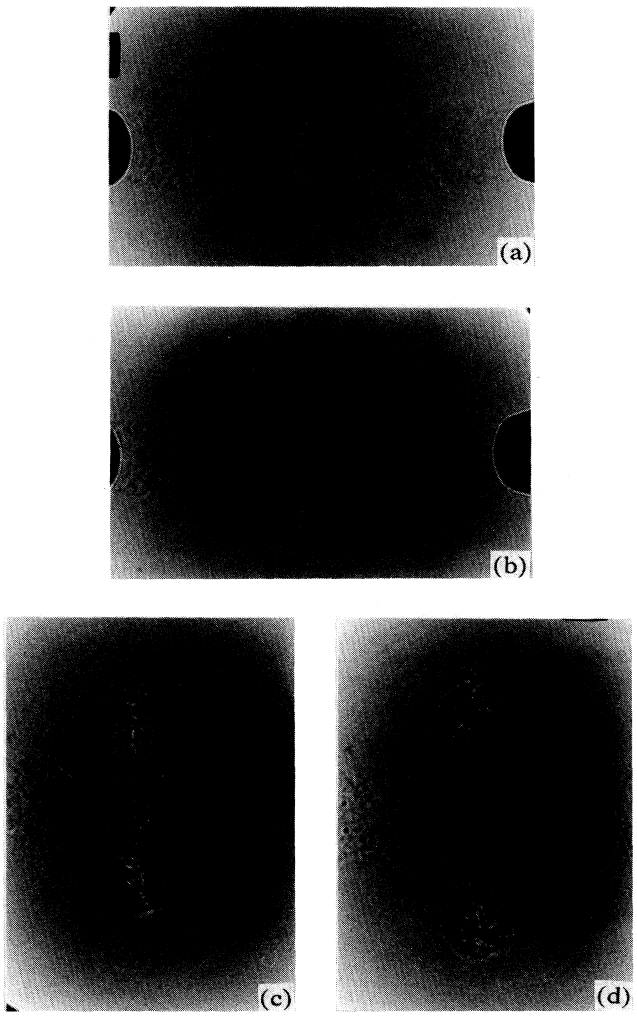

FIG. 15. Shadowgraphs of the rear view (viewed from the positive y_3 direction) of the collision of two vortex rings: (a) 0 μs, (b) 20 μs, (c) 30 μs, and (d) 50 μs [relative time from the instant (a)].

A remarkable property obtained in the experiment is the asymmetric emission represented by the mode P_3^0. Its effect is seen in Figs. 8 and 9 at the times marked by α and β. This is considered in the next section.

VI. SIGNIFICANCE OF THE DOMINANT MODES AND ASYMMETRIC EMISSION

Observed amplitudes A_1 and A_2 of the two quadrupoles P_2^0 and $P_2^2\cos(2\phi)$ in (29) are substantially large and there exists non-negligible amplitude of the monopole in the observation (Fig. 7). By the theory developed in Sec. II, the amplitudes $A_1(t)$ and $A_2(t)$ are represented in terms of three longitudinal quadrupoles Q_{11}, Q_{22}, Q_{33} (to the directions x_1, x_2, x_3), as understood from the form of the coefficients of F_2 in Eq. (26).

Out of the two third-order components, the amplitude B_2 of the mode $P_3^2\cos(2\phi)$ is negligibly small, but the appearance of the mode P_3^0 is substantial. To see the significance of these modes, we examine their amplitudes B_1 and B_2. From Eq. (30c), the amplitude $B_1(t)$ is proportional to the fourth-order time derivative of the following integral:

$$Q_{333}(t) - \tfrac{1}{5}Q_{3kk}(t) = \frac{1}{32\pi}\int 2p_3(\mathbf{y},t)\,(y_3^2 - y^2)\,d^3\mathbf{y}\ , \tag{32}$$

where

$$2p_3(\mathbf{y},t) = y_1\omega_2 - y_2\omega_1 \equiv \mathbf{y}_*\wedge\boldsymbol{\omega}_*\ ,$$
$$\mathbf{p} = \frac{1}{2}\mathbf{y}\times\boldsymbol{\omega}\ ,$$

the vectors $\mathbf{y}_* = (y_1, y_2)$ and $\omega_* = (\omega_1, \omega_2)$ being projections of $\mathbf{y}$ and ω on the plane (x_1, x_2). Similarly the amplitude $B_2(t)$ is proportional to the fourth-order time derivative of the integral,

$$\tilde{Q}_{113}(t) - \tilde{Q}_{223}(t) = \frac{1}{32\pi}\int[2p_3(y_1^2 - y_2^2) + 4(p_1y_1 - p_2y_2)y_3]\,d^3\mathbf{y}\ , \tag{33}$$

which does not vanish due to an asymmetry in the (x_1, x_2) plane. However, its contribution to the wave profile is reduced by the factor 1/30 multiplied to the above integral as given in Eq. (30d). In fact, the amplitude B_2 is very small in both the observation and the simulation.

As seen from Eq. (32), the amplitude $B_1(t)$ is related to the distribution of $\mathbf{p} = \frac{1}{2}\mathbf{y}\times\boldsymbol{\omega}$, the impulse density of the vortex system. The total impulse $P_i^{(v)}=4\pi Q_i$ defined by the space integral of $p_i(\mathbf{y},t)$ is conserved in the vortex motion in free space (an analogue in the vortex system to the momentum conservation). Integrating $\mathbf{p}(\mathbf{y},t)$ over a large volume V and taking the time derivative, one has

$$\frac{d}{dt}\mathbf{P}^{(v)} = \tfrac{1}{2}\int_V \mathbf{y}\times\partial_t\boldsymbol{\omega}\,d^3\mathbf{y}\ . \tag{34}$$

Using Eq. (6), the integrand in RHS is expressed as $2\mathbf{v}\times\omega$ plus several terms in the form of space derivatives, and these derivatives yield surface integrals over S surrounding the volume V which vanish in the limit as the surface S recedes to infinity. Further, the ith component of $\mathbf{v}\times\omega$ is expressed as $\partial_k(\frac{1}{2}v^2\delta_{ik} - v_i v_k)$ and its volume integral is again transformed to vanishing surface integrals. Thus the RHS of Eq. (34) vanishes identically. The invariance of $Q_i(= P_i^{(v)}/4\pi)$ leads to the absence of dipole emission in the present case.

We now consider the case of head-on collision of two vortex rings to see the significance of the impulse density $\mathbf{p}$. Suppose that two identical, but opposite sense of circular vortex rings are located in the two planes $x_3 = \pm Z$ at symmetrical positions with respect to the plane $x_3 = 0$ and their centers being on the x_3 axis, and that they approach the symmetry plane $x_3 = 0$ in due course by their own motions. By the symmetry of the vorticity distribution, it is immediately verified that the two integrals of Eqs. (32) and (33) vanish identically. Therefore the third-order modes B_1 and B_2 disappear in the head-on collision. The only remaining quadrupole is $P_2^0(\cos\theta)$ because we have

$$Q_{11} = Q_{22}\ , \quad Q_{33}(t) = -\frac{1}{12\pi}\int p_3 y_3\, d^3\mathbf{y} \neq 0\ . \qquad (35)$$

Thus the acoustic emission by the head-on collision of two vortex rings is given by $A_0(t) + A_1(t)P_2^0(\cos\theta)$, with up-down symmetry along the x_3 axis as well as the x_1–x_2 symmetry, which is the case studied by Ref. [7]. The oblique collision studied here has neither the up-down symmetry nor the x_1-x_2 symmetry. The former asymmetry is represented by $B_1(t)P_3^0(\cos\theta)$ and the latter by $A_2(t)P_2^2(\cos\theta)\cos 2\phi$.

It is remarkable that the amplitudes $A_1(t)$ and $B_1(t)$ depend on the spatial distribution and temporal evolution of only the component $p_3(\mathbf{y},t)$ [see Eqs. (32), (35), and (30)]. In particular very rapid change of $p_3(\mathbf{y},t)$ will give rise to enhancement of the amplitude $B_1(t)$, since it is proportional to the fourth-order time derivative of Eq. (32). Restricting our attention to the location of the vortex line reconnection at the inner part C_i and reminding the geometry of the vortex lines (Fig. 16), the variable p_3 (near $\mathbf{y}_* = 0$) is found to be positive before the reconnection and vanish when the antiparallel vortex lines cancel by the viscous effect. Its rapid change will give substantial contribution to the terms $Q^{(4)}_{333}(t)$ and $Q^{(4)}_{3kk}(t)$. Similarly from the outer part C_o there is another substantial contribution. In this regard, notice that local fluid is driven upward energetically by the vortex-pair configuration (characterized by antiparallel vortex lines) formed before reconnection at the inner part [Figs. 14(a), 14(b), 15(a), and 15(b); the trajectory C_i of Fig. 2], and then local downward motion is excited by subsequent collision of the outer part [Figs. 14(c), 14(d), 15(c), and 15(d); the trajectory C_o of Fig. 2]. The first inner-part collision generates the upward emission around the time α and the second outer-part collision generates the downward emission around the time β. The formation of vortex-pair configuration before reconnection is referred to as *collapse* (to antiparallel configuration) in the recent article [26] on high-performance computer visiometrics. In the present case the antiparallel configuration at the inner part occurs naturally by the initial setup of two vortex rings.

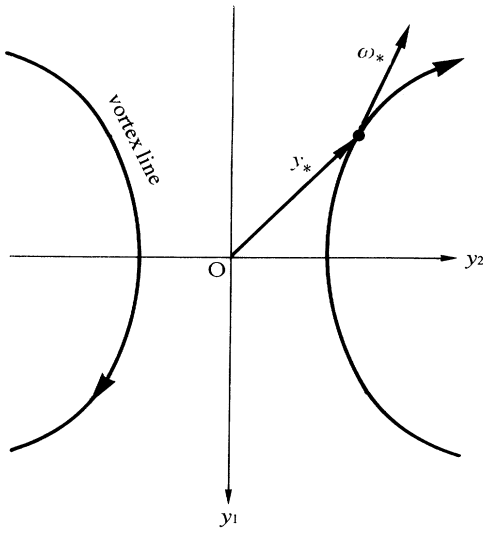

FIG. 16. Schematic illustration of the geometry of vortex lines just before reconnection.

Thus, the significant amplitude $B_1(t)$ observed in the experiment (see Fig. 7) is representing an acoustic signal of local energetic motions excited by the collision. The observed acoustic pressure exhibits a characteristic asymmetry of the directivity at the times when the P_3^0 mode is significant.

It is confirmed in the computer simulation (but not shown here) that there exist two regions in space which contribute to $(d/dt)^2 Q_{333}$: one is near the place of reconnection (along the trajectory C_i of Fig. 2) but shifted slightly upward (to the positive y_3 direction), and the other is near the trajectory C_o, but shifted slightly downward (to the negative y_3 direction). The former part gives positive contribution, but disappears soon, while the latter one gives both negative and positive contributions with the negative one dominating and continues to exist after the time b. In regard to the property mentioned earlier (in the beginning of Sec. V) that the positive B_1 pulse is located between the times a and b, we note that the time derivative in $A_1(t)$ is third order, while that in $B_1(t)$ is fourth order.

Thus it is found that the up-down asymmetry of radiation at the times α and β is related to the energetic motion excited by the oblique collision, in which the reconnection of vortex lines is occurring.

VII. CONCLUSION

A general mathematical formulation for the acoustic wave generated by a vortex motion is presented. The acoustic field is expressed in the form of multipole expansions and the far-field pressure is represented by a linear

combination of the spherical harmonics on a sphere of observation. The isotropic component of wave pressure (monopole) is proportional to the time derivative of the energy dissipation rate. The components of the second-order terms (the quadrupoles) and of higher-order terms are related to the time development of moments of the vorticity distribution.

This formulation is applied to the case of oblique collision of two vortex rings, which is a source of the sound emission. The vortex motion is influenced by the viscosity. Reconnection and merging of vortices in the collision process of two vortex rings are simulated numerically by solving the Navier-Stokes equation and the continuity equation. The components of acoustic pressure have been calculated by using the computed vorticity distribution, based on the mathematical expressions developed in the present paper.

Apart from the numerical simulation, laboratory experiments for this problem have been made independently. The trajectories of the vortex cores were observed optically. The acoustic pressures were measured in the far-field on the three orthogonal planes. The main modes of the acoustic radiation are the two quadrupoles which are expressed by two second-order spherical harmonics. The third-order mode (which is not usually discussed in the literatures) has been found to be significant with the amplitude which is of the same order as the two quadrupoles at and after the time when the vortex cores begin to touch each other. This exhibits a characteristic emission of up-down asymmetry.

Comparison has been made between the acoustic modes obtained in the experiment and those of the numerical simulation. It is found that the profiles are qualitatively in agreement. However, the numerical mode amplitudes are much smaller than the observed ones and the time scale of the numerical profiles is larger. These quantitative differences of the profiles may be attributed to the difference in magnitude of the characteristic Reynolds numbers.

These studies are *juxtaposed* [26] with an additional optical observation by shadowgraphs to see the collision process. Remarkable similarity is found for the morphology and time evolution of the vortex collision between the experimental observation and the computer simulation.

In addition, the shadowgraphs exhibit traces of wave generation, which will be observed as acoustic waves in the far field. This is consistent with the following view. The characteristic asymmetric emission of the acoustic waves is found at the times when the third-order mode $B_1(t)$ is substantial. Based on the mathematical analysis, this is interpreted as representing the acoustic signal of the local energetic fluid motion related to the collision, reconnection, and subsequent motion of vortices.

ACKNOWLEDGMENTS

The authors are grateful to Professor T. Murakami for his kind cooperation during the experiment. One of the authors (M.T.) would like to acknowledge Professor S. Kida and Professor F. Hussain. The computation was done on the FACOM M780/30-VP400E system in the data processing center of Kyoto University.

APPENDIX: DERIVATION OF EQS.(9)–(11)

We are going to show here that, starting from

$$v_i = \epsilon_{ijk}\, \partial_j A_k \ ,$$

where A_k is given by (7), we obtain

$$v_i = \partial_i \Phi \quad , \quad \Phi = \sum_{n=1}^{\infty} \Phi_n \ ,$$

where Φ_n is given by (10).

In fact, in view of the assumed localized distribution of the vorticity $\boldsymbol{\omega}(\mathbf{y}, t)$ satisfying $\boldsymbol{\nabla} \cdot \boldsymbol{\omega} = 0$, we have the following identity:

$$\begin{aligned} 0 &= \int \boldsymbol{\nabla} \cdot (\boldsymbol{\omega}\ y_k y_{p_1} \cdots y_{p_n})\, d^3\mathbf{y} \\ &= \int [\omega_k\, y_{p_1} \cdots y_{p_n} + y_k \omega_{p_1} y_{p_2} \cdots y_{p_n} + \cdots + y_k y_{p_1} \cdots y_{p_{n-1}} \omega_{p_n}] d^3\mathbf{y} \\ &= W^k_{p_1 \cdots p_n} + W^{p_1}_{k\, p_2 \cdots p_n} + \cdots + W^{p_n}_{k\, p_1 \cdots p_{n-1}} \\ &= W^k_{p_1 \cdots p_n} + \sum_{[p_1, \ldots, p_n]} W^{p_1}_{k\, p_2 \cdots p_n} \end{aligned} \tag{A1}$$

where $W^k_{p_1 \cdots p_n}$ is defined by (8), the summation in the second term of the last expression is understood to take all the cyclic permutation of $(p_1, \ldots, p_n)$ with k fixed (all the indices take values on the integers 1, 2, and 3).

Hence from (7) we have

$$\begin{aligned} v_i &= \epsilon_{ijk} \partial_j A_k \\ &= \frac{1}{4\pi} \sum_{n=1}^{\infty} \frac{(-1)^n}{n!} \sum_{p_1} \cdots \sum_{p_n} \varepsilon_{ijk} W^k_{p_1 \cdots p_n} \partial_j \partial_{p_1} \cdots \partial_{p_n} \frac{1}{r} \ . \end{aligned} \tag{A2}$$

We introduce

$$C_{s\,t_1\cdots t_{n-1}} = \int (\mathbf{y}\times\boldsymbol{\omega})_s\, y_{t_1}\cdots y_{t_{n-1}} d^3\mathbf{y} = \epsilon_{spq}\, W^q_{p\,t_1\ldots t_{n-1}} \,. \tag{A3}$$

We multiply the $C_{s\,t_1\cdots t_{n-1}}$ with ϵ_{skl} and take the sum with respect to s,

$$\epsilon_{skl}C_{s\,t_1\cdots t_{n-1}} = \epsilon_{skl}\,\epsilon_{spq}W^q_{p\,t_1\ldots t_{n-1}} = W^l_{k\,t_1\ldots t_{n-1}} - W^k_{l\,t_1\ldots t_{n-1}} \,.$$

Here we take the sum of (A3) for cyclic permutation of the indices $(l, t_1, \cdots, t_{n-1})$ with k fixed,

$$\sum_{[l,t_1,\ldots,t_{n-1}]} \epsilon_{skl}C_{s\,t_1\cdots t_{n-1}} = \sum_{[l,t_1,\ldots,t_{n-1}]} W^l_{k\,t_1\ldots t_{n-1}} - n\, W^k_{l\,t_1\ldots t_{n-1}} = -(n+1)\, W^k_{l\,t_1\ldots t_{n-1}} \,.$$

The second equality is obtained by the help of (A1). Multiplying this with ϵ_{ijk} and taking contraction with respect to k, we obtain

$$\epsilon_{ijk}W^k_{p_1\ldots p_n} = -\frac{1}{n+1}\sum_{[p_1,\ldots,p_n]} \epsilon_{ijk}\epsilon_{p_1 sk}C_{s\,p_2\cdots p_n} = -\frac{1}{n+1}\sum_{[p_1,\ldots,p_n]} [\, C_{j\,p_2\cdots p_n}\delta_{ip_1} - C_{i\,p_2\cdots p_n}\delta_{jp_1}\,] \,.$$

Thus, substituting this in (A2), we obtain

$$v_i = \frac{1}{4\pi}\sum_{n=1}^{\infty}\frac{(-1)^{n+1}}{(n+1)!}\sum_{[p_1,\ldots,p_n]}\sum_j\sum_{p_2}\cdots\sum_{p_n}\left[C_{j\,p_2\cdots p_n}\delta_{ip_1}\partial_j\partial_{p_1}\partial_{p_2}\cdots\partial_{p_n}\frac{1}{r} - C_{i\,p_2\cdots p_n}\partial_{p_2}\cdots\partial_{p_n}\partial_j^2\frac{1}{r}\right] . \tag{A4}$$

Since $\partial_j^2\,(1/r) = 0$ (for $r \neq 0$), the second term in the brackets [] vanishes. Further, noting the relation

$$\sum_{[p_1,\ldots,p_n]}\sum_{p_1}\sum_{p_2}\cdots\sum_{p_n} = n\sum_{p_1}\sum_{p_2}\cdots\sum_{p_n} \,,$$

and $\delta_{ip_1}\,\partial_{p_1} = \partial_i$, we finally find the expressions (9)–(11) in the main text from (A4), where the suffix j is written as p_1.

[1] A. Powell, J. Acoust. Soc. Am. **36**, 177 (1964).
[2] F. Obermeier, Acustica **18**, 238 (1967).
[3] V.R. Lauvstad, J. Sound Vib. **7**, 90 (1968).
[4] S.C. Crow, Stud. Appl. Math. **49**, 21 (1970).
[5] M.S. Howe, J. Fluid Mech. **71**, 625 (1975).
[6] W. Möhring, J. Fluid Mech. **85**, 685 (1978).
[7] T. Kambe and T. Minota, Proc. R. Soc. London, Ser. A **386**, 277 (1983).
[8] T. Kambe, J. Fluid Mech. **173**, 643 (1986).
[9] E.-A. Müller and F. Obermeier, Fluid Dyn. Res. **3**, 43 (1988).
[10] T. Minota and T. Kambe, J. Sound Vib. **111**, 51 (1986).
[11] T. Kambe, T. Minota, T. Murakami, and M. Takaoka, *Topological Fluid Mechanics*, edited by H.K. Moffatt and A. Tsinober (Cambridge University Press, Cambridge, England, 1990), pp. 515–524.
[12] T. Minota, T. Kambe, and T. Murakami, Fluid Dyn. Res. **3**, 357 (1988).
[13] T. Minota, T. Murakami, and T. Kambe, Fluid Dyn. Res. **4**, 57 (1988).
[14] G.E.A. Meier, H.-M. Lent, and K.F. Löhr, Fluid Dyn. Res. **3**, 344 (1988).
[15] M.J. Lighthill, Proc. R. Soc. London, Ser. A **211**, 564 (1952).
[16] T. Kambe and T. Minota, J. Sound Vib. **74**, 61 (1981).
[17] G.K. Batchelor, *An Introduction to Fluid Dynamics* (Cambridge University Press, Cambridge, England, 1967), Chaps. 2 and 6.
[18] T. Kambe, J. Sound Vib. **95**, 351 (1984).
[19] F. Obermeier, J. Sound Vib. **99**, 111 (1985).
[20] N. Curle, Proc. R. Soc. London, Ser. A **231**, 505 (1955).
[21] T. Kambe, T. Minota, and Y. Ikushima, J. Fluid Mech. **155**, 77 (1985).
[22] S. Kida, M. Takaoka, and F. Hussain, Phys. Fluids A **1**, 630 (1989); see also J. Fluid Mech. **230**, 583 (1991).
[23] S.A. Orszag, Stud. Appl. Math. **50**, 293 (1971).
[24] P.G. Saffman, Stud. Appl. Math. **49**, 371 (1970).
[25] T. Kambe and U Mya Oo, J. Phys. Soc. Jpn. **53**, 2263 (1984).
[26] N.J. Zabusky, D. Silver, R. Pelz, and Vizgroup'93, Physics Today **46** (3), 24 (1993).
[27] T. Kambe, *Theoretical and Applied Mechanics, 1992*, edited by S. R. Bodner, J. Singer, A. Solan, and Z. Hashin (Elsevier Science, Amsterdam, 1993), pp. 239–255.

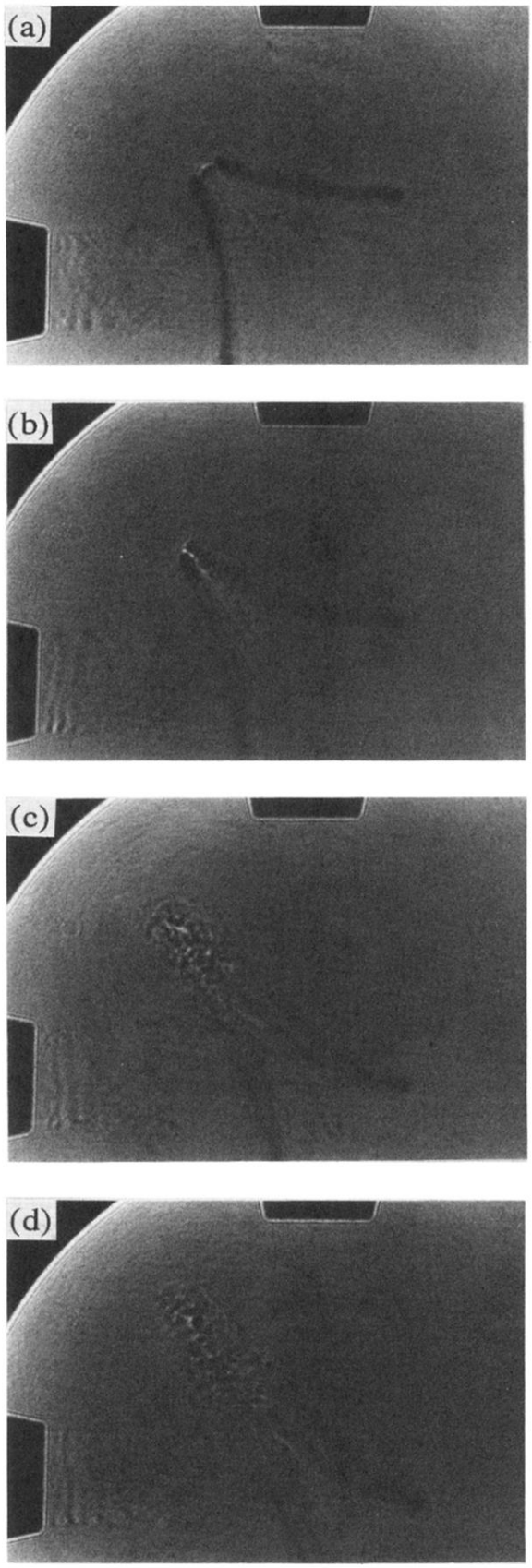

FIG. 14. Shadowgraphs of the side view of the collision of two vortex rings at a higher vortex speed than that of the acoustic measurement: (a) 0 μs, (b) 20 μs, (c) 40 μs, and (d) 60 μs [relative time from the instant (a)].

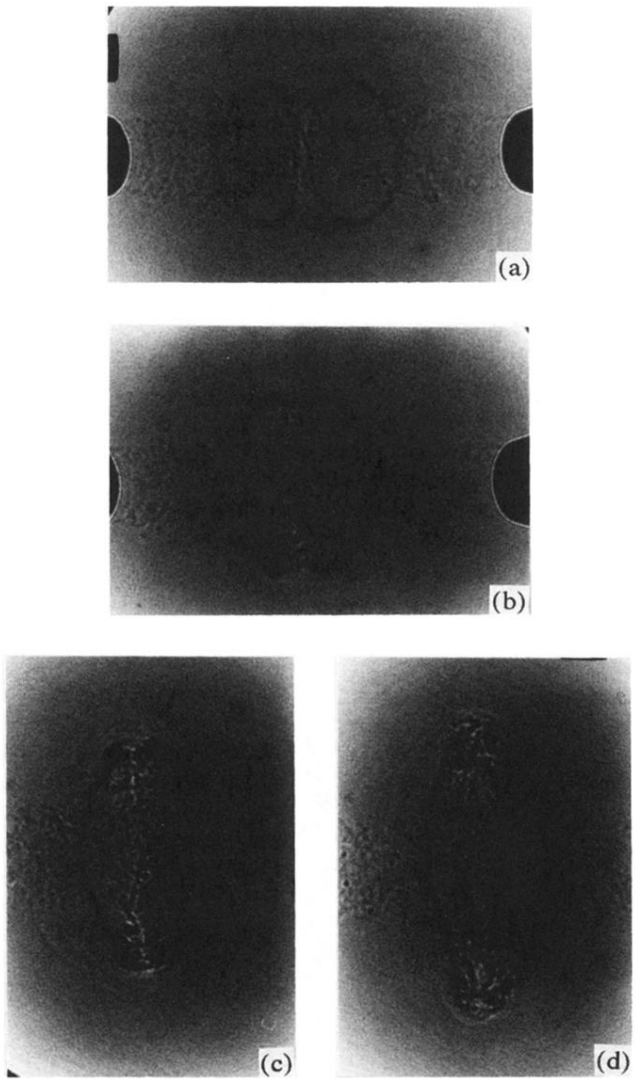

FIG. 15. Shadowgraphs of the rear view (viewed from the positive y_3 direction) of the collision of two vortex rings: (a) 0 μs, (b) 20 μs, (c) 30 μs, and (d) 50 μs [relative time from the instant (a)].